APPLIED SCIENCES AND ENGINEERING

Highly anisotropic and flexible piezoceramic kirigami for preventing joint disorders

Ying Hong[1]*, Biao Wang[1]*, Weikang Lin[1], Lihan Jin[1], Shiyuan Liu[1], Xiaowei Luo[2], Jia Pan[3], Wenping Wang[3,4], Zhengbao Yang[1,5]†

The prevention of work-related upper extremity musculoskeletal disorders (MSDs; e.g., neck pain and shoulder fatigue) requires frequent exercises of neck and shoulder that primarily rely on the assistance of joint motion monitoring devices. However, most available wearable healthcare sensors are rigid, bulky, and incapable of recognizing the full range of human motions. Here, we propose a kirigami-structured highly anisotropic piezoelectric network composite sensor that is able to monitor multiple information of joint motions, including bending direction, bending radius, and motion modes, and to distinguish them simultaneously within one sensor unit. On the basis of the modified template-assisted processing method, we design a functional piezoceramic kirigami with a honeycomb network structure that is stretchable (~100% strain), highly sensitive (15.4 mV kPa^{-1}), and highly anisotropic to bending directions (17.3 times from 90° to 0°). An integrated monitoring system is further established to alarm the prolonged sedentary behaviors, facilitating the prevention of upper extremity MSDs.

INTRODUCTION

Work-related upper extremity musculoskeletal disorders (MSDs) have given rise to various problems such as declining life quality, increased risk of rheumatoid arthritis, and reduced work productivity, which attract extensive attention these years (*1*, *2*). It is estimated that approximately 100 million European citizens suffer from MSDs, and the total cost attributable to MSDs could be as high as 2% of gross domestic product (GDP) (*3*). Among the MSDs, neck pain and shoulder fatigue, associated with prolonged sedentary postures with insufficient variation during computer-intensive office work, become the most reported symptoms that occupy 25% of the MSDs patients (*4*–*6*). Therefore, it is urgent to develop a monitoring system that can continuously monitor the joint movements during daily activities for the prevention and rehabilitation of upper extremity MSDs (*7*). Multifarious monitoring systems have been proposed to obtain motion signals of joints such as wrist, knee, and ankle, mostly executed by wearable sensors including inertial sensors, strain gauges, accelerometers, and optical fiber sensors (*7*, *8*). However, most currently available systems suffer from complex and rigid sensor structure (usually, measurement range < 5% strain), computationally complex data processing, and inadequate motion information acquisition (only unidirectional deformation), restricting their practical applications.

Recently, the development of flexible electronics has greatly facilitated the application of wearable healthcare sensors in monitoring physiological information (*9*–*18*), such as human motion (*19*–*22*), body temperature (*17*, *23*), heartbeat (*24*–*27*), respiration (*24*, *25*), and sweat (*28*–*30*). Among these, flexible piezoelectric sensors with an electrical response to mechanical deformation have the advantages of rapid response speed and high sensitivity, which make them promising candidates for monitoring physiological information (*31*–*37*). However, as one of the most important synovial (freely movable) joint motions, neck and shoulder motions have complex motion modes with various joint angles, joint directions, and postures (*7*). Most flexible piezoelectric sensors are neither stretchable nor multifunctional, which is not enough to detect the joint movements with large strain and multiple degrees of freedom. To achieve the desirable stretchability, besides the introduction of composite with intrinsic elasticity, stretchable structure designs are needed (*33*).

Kirigami, the ancient art of cutting paper, shows a great ability to transfer structures from stiff to stretchable forms because of the free rotation and buckling of the cut units without damaging the individual units (*38*). As a result, kirigami structure has been widely used as passive substrates or electrodes for elastic composites (*39*), stretchable electronics (*33*, *40*), deformable batteries (*41*), and optical devices (*38*). Here, we present a functional kirigami. Instead of using it as passive substrates, we fabricate active kirigami piezoceramic and use it as the functional skeleton of physiological sensors. The unit cells formed by functional piezoceramic also allows for the dimensional anisotropy coming from selected kirigami geometries (*33*).

On the basis of the functional kirigami, we propose a kirigami-structured highly anisotropic piezoelectric network composite (HAPNC) sensor that is capable of monitoring joint motions and distinguishing between different motion modes. We present a modified template-assisted sol-gel method for fabricating flexible piezoceramic composites and design a two-dimensional (2D) honeycomb piezoceramic kirigami as the core sensor element. The designed kirigami structure not only improves the piezoelectric properties due to the increased connectivity of the piezoceramic phase but also provides the desired high-dimensional anisotropy. Using this anisotropy, we can measure the stress from any direction in a plane, obtaining the stress amplitude and direction at the same time. In addition, the dimensional extension of the HAPNC sensor also allows us to obtain information about motion modes of joints. A monitoring and alarm system is further established to monitor the joint motions of the neck and shoulder, alarming about the prolonged sedentary behavior.

[1]Department of Mechanical Engineering, City University of Hong Kong, Hong Kong, China. [2]Department of Architecture and Civil Engineering, City University of Hong Kong, Hong Kong, China. [3]Department of Computer Science, University of Hong Kong, Hong Kong, China. [4]Department of Computer Science and Engineering, Texas A&M University, College Station, TX 77843, USA. [5]City University of Hong Kong, Shenzhen Research Institute, Shenzhen 518057, China.
*These authors contributed equally to this work and share first authorship.
†Corresponding author. Email: zb.yang@cityu.edu.hk

RESULTS

Structure and fabrication of the HAPNC sensor

As illustrated in Fig. 1A, the HAPNC sensors are attached to the skin surface of the neck and shoulder to monitor joint motions and help the prevention of upper extremity MSDs. The joint movements lead to the deformation of the HAPNC sensors, which simultaneously converts into electrical signals due to the direct piezoelectric effect. The produced electrical signals are then continuously transmitted to the intelligent terminal (i.e., computers) through a microcontroller for data storage and analysis (e.g., identifying the motion modes of neck from the output signals as shown in Fig. 1B). The multilayer HAPNC sensor consists of a cross-shaped polyethylene terephthalate (PET) substrate (4 cm × 4 cm), a square top sensor, and a square bottom sensor (1.5 cm × 1.5 cm). Both the top and bottom sensors are composed of two electrodes and one piezoelectric composite. The piezoelectric composite is the core sensory element for the sensors, formed by a lead zirconate titanate (PZT) ceramic network with kirigami-structured honeycomb grids and a polydimethylsiloxane (PDMS) matrix.

Different from many of the previous arts using kirigami as passive substrates, here, we use kirigami itself as functional units. The anisotropy of the composite comes from the unique honeycomb kirigami structure and can be controlled by carefully designing its geometry. To sense bending direction and bending radius, we arrange the piezoceramic network between the top and bottom sensors into perpendicular alignment. In addition, the dimensional extension of the HAPNC sensor also allows us to obtain information about deformation modes of the joint, benefiting the monitoring of MSDs (Fig. 1B). The optical image of the HAPNC sensor is shown in Fig. 1C. The HAPNC sensor is highly flexible and can be easily attached to the skin surface of human joints, i.e., neck, shoulder, elbow, and wrist, without any discomfort (Fig. 1D).

Figure 2A illustrates the manufacturing process of the kirigami-structured piezoelectric network composite using the modified template-assisted sol-gel method, which is effective in manufacturing piezoelectric composite with interconnected piezoceramic phase (*42*, *43*). First, the prepared mixed PZT suspensions are dropped onto the stretched organic textile with honeycomb grids until the whole organic textile template is immersed by the mixed suspensions. After hot air drying, the precursor is then sintered to remove the organic textile template. In the manufacturing process, the sintered PZT ceramic network keeps a similar stretched honeycomb morphology as the original textile template without obvious volume shrinkage. The obtained PZT ceramic network is infiltrated with the uncured PDMS spin-coated on the surface of the indium tin oxide (ITO) film with PET substrate to form the piezoelectric network composite. With two layers of piezoelectric composites constructed step by step and silver nanowires (Ag NWs) sprayed as the electrodes, the multilayer HAPNC sensor is finally obtained (detailed manufacturing process can be found in figs. S1 and S2 and text S1).

Because the anisotropy of the piezoelectric composite is determined by the honeycomb grids, we can change the anisotropic property by controlling the prestrain of the stretched organic textile template with honeycomb grids. Compared with the complex alignment process of 1D fiber-reinforced composite, the proposed method guarantees the uniformity and stabilization of the piezoelectric reinforced materials. Figure 2 (B to D) shows the scanning electron microscopic images of the PZT ceramic network based on the organic textile templates with 0, 10, and 20% prestrain, respectively.

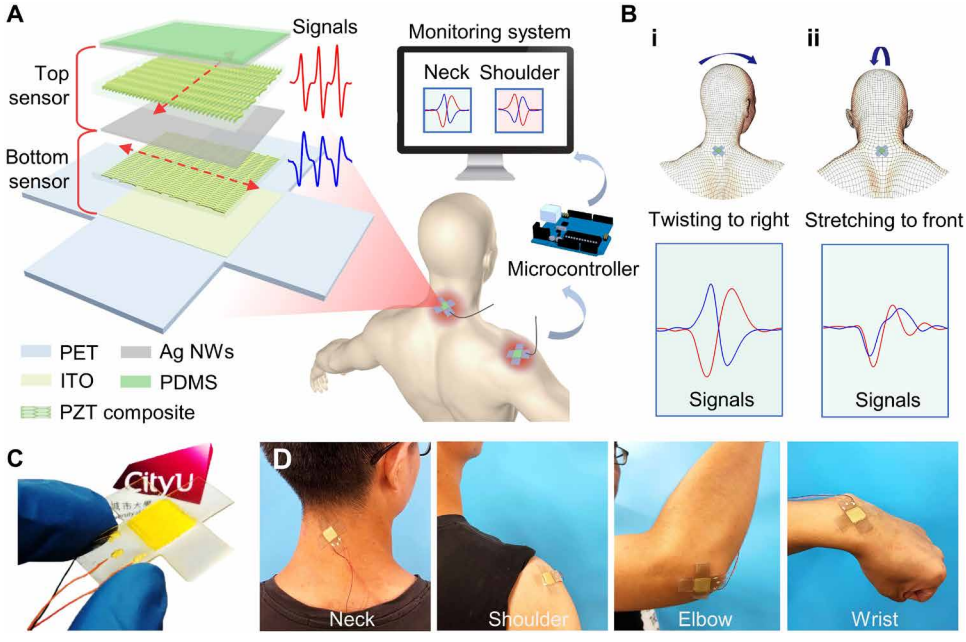

Fig. 1. Structure and working mechanism of the kirigami-structured HAPNC sensor. (**A**) Schematic illustration of the system to monitor MSDs. The signals produced from the attached sensors are transmitted to an intelligent terminal through a microcontroller for further analysis. The multilayer HAPNC sensor consists of a cross-shaped polyethylene terephthalate (PET) substrate, a square top sensor, and a square bottom sensor. (**B**) Two typical signals of the HAPNC sensor used to distinguish the neck movements, including twisting to right and stretching to front. (**C**) Optical image of the HAPNC sensor. (**D**) Optical images of the HAPNC sensor attached to neck, shoulder, elbow, and wrist, showing the high flexibility of the sensor and its compatibility with joints. Photo credit: Ying Hong, City University of Hong Kong.

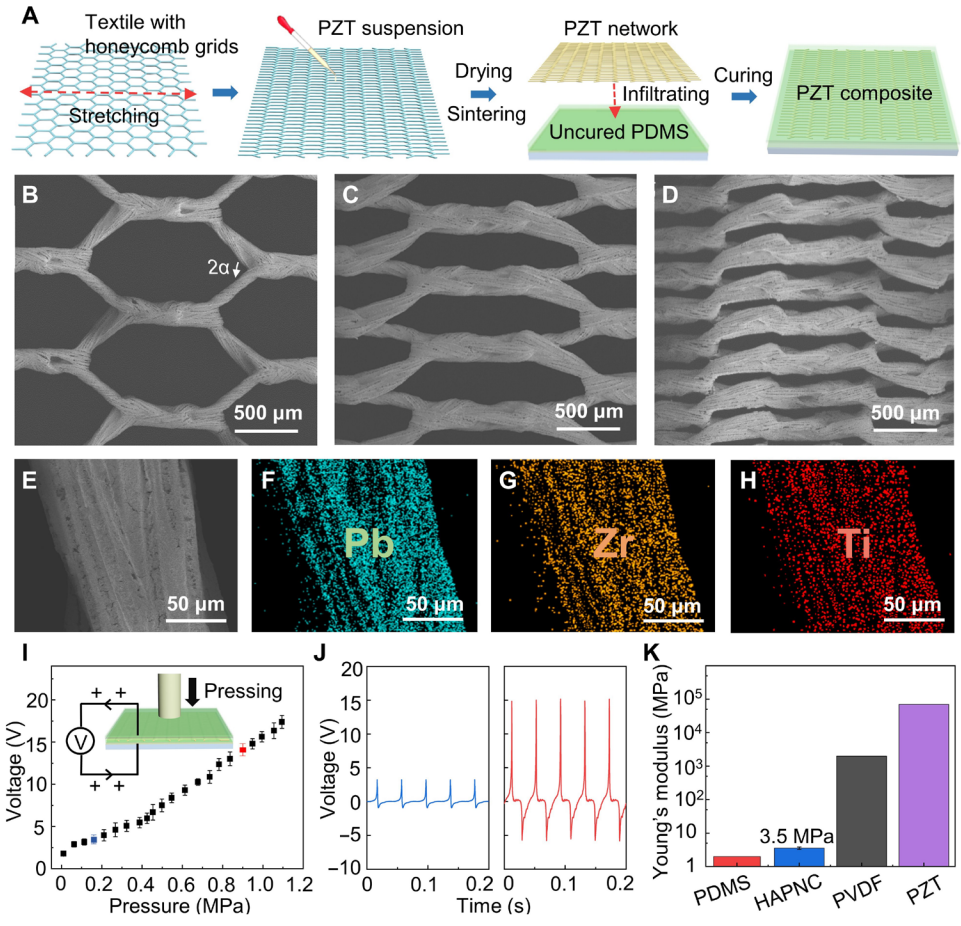

Fig. 2. Fabrication and fundamental characterization of the kirigami-structured piezoelectric composite. (**A**) Illustration of the manufacturing process of the kirigami-structured piezoelectric composite. (**B** to **D**) Scanning electron microscopic images of the PZT ceramic network based on the textile templates with a prestrain of (B) 0%, (C) 10%, and (D) 20%, respectively. With the prestrain increasing, a considerable improvement of the degree of alignment for the PZT ceramic network is achieved, thus enhancing the anisotropy. (**E** to **H**) Energy-dispersive spectroscopy mapping of the PZT ceramic network. The elements of lead, zirconium, and titanium are homogeneously dispersed in the ceramic network. (**I**) Average voltage peaks of the piezoelectric composite under compressing pressure from 30 kPa to 1.1 MPa. The piezoelectric composite shows both a high sensitivity of 15.4 mV kPa^{-1} and a high linearity. The load frequency is 25 Hz. Inset shows the current direction during the compression process. (**J**) Two typical voltage signals of the piezoelectric composite under the pressure of 0.15 and 0.9 MPa, respectively. (**K**) Comparison of the Young's modulus of the piezoelectric composite with PDMS, poly(vinylidene fluoride) (PVDF), and PZT.

As prestrain increases from 0 to 20%, the grid angle α of the honeycomb network decreases from 45° to 15°, revealing a remarkable improvement of the degree of alignment of the PZT ceramic network. From Fig. 2D and fig. S3A, we can also observe the intact network connection of the PZT ceramic network with an increased piezoceramic phase, which endows the HAPNC with both a high piezoelectric sensitivity (15.4 mV kPa^{-1}) and a high linearity (R^2 = 0.98) compared to the composite with randomly dispersed fillers (Fig. 2, I and J, and fig. S4) (*42*–*44*). Besides, the multistrand and hollow structure of the PZT ceramic network (fig. S3) allows the infiltration of PDMS and improves the stretchability of the piezoelectric composite with Young's modulus ~3.5 MPa close to pure PDMS (Fig. 2K). Accompanied by the designed kirigami structure, the piezoelectric composite shows a maximum strain of ~100% (fig. S5), which enables the HAPNC sensor to detect the stretching and contraction movements of human joints with strain as high as 55% (*16*).

To further enhance the piezoelectric responses, we add PZT powders in the preparation of PZT sol-powder suspension, greatly increasing the effective mass of the PZT ceramic network in the composite. On the other hand, the introduction of PZT powders will not destruct the perovskite structure of the PZT ceramic network, which is confirmed through the x-ray diffraction patterns (fig. S6A) and the Raman spectrum (fig. S6B). Furthermore, the energy-dispersive spectroscopic mapping (Fig. 2, E to H) shows that the elements of Pb, Zr, and Ti are homogeneously distributed in the ceramic network without irrelevant elements (detailed characterization information can be found in text S2).

Anisotropic piezoelectric responses of the S-HAPNC sensor

To reveal the anisotropic piezoelectric properties of the HAPNC sensor, we first investigate the effects of the bending direction and the bending radius on the piezoelectric responses from the HAPNC sensor with single-layer piezoelectric composite (S-HAPNC). Here, we define the angle between the alignment direction and bending direction as bending angle θ and the minimum curvature radius of the device during the bending process as bending radius *r*, as shown in Fig. 3A.

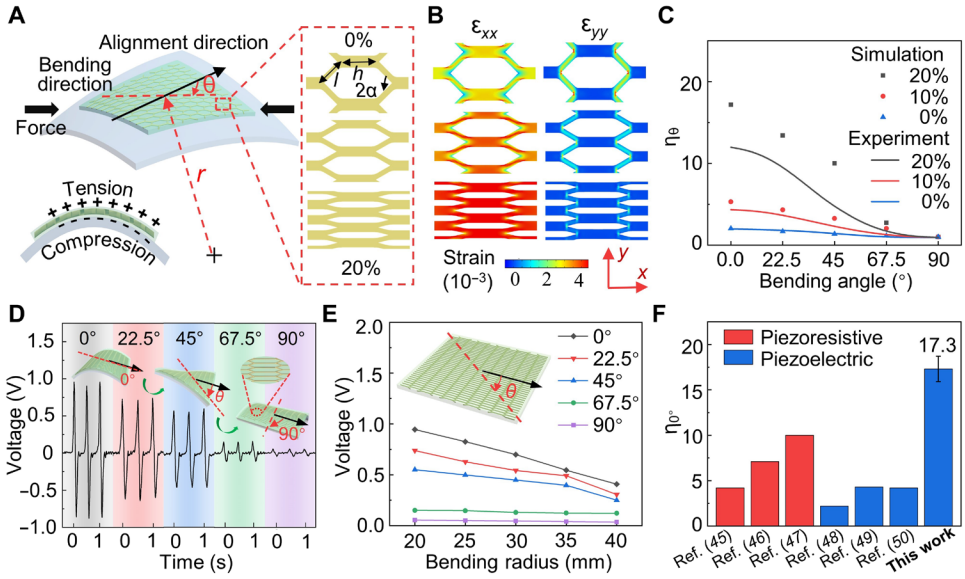

Fig. 3. Piezoelectric responses of the S-HAPNC sensor. (**A**) Illustration showing the bending angle and the bending radius of the S-HAPNC sensor with different networks. Inset shows the charge distribution during the bending process. (**B**) Simulation (FEA) results showing the strain distributions of the ceramic network under 0° and 90° bending angle for three different geometric parameters with 0, 10, and 20% prestrain. The bending radius is 20 mm. (**C**) Simulation and experimental results of the piezoelectric anisotropy η_θ of the S-HAPNC sensor for three different geometric parameters. The bending radius is 20 mm. (**D**) Experimental results of the open-circuit voltage signals from the S-HAPNC sensor with 20% prestrain geometry under different bending angles. The bending radius is 20 mm. (**E**) Experimental results of the average voltage peaks (error < 5%) from S-HAPNC sensor with 20% prestrain geometry under different bending radii and different bending angles. It shows that the anisotropy is enhanced for the 20% prestrain case. (**F**) Comparison of the developed HAPNC sensor with the existing anisotropic sensors. The HAPNC demonstrates a high anisotropy of ~17.3.

To quantify the piezoelectric anisotropy of the S-HAPNC sensor, we define η_θ as

$$\eta_\theta = \frac{V_\theta}{V_{90^\circ}} \quad (1)$$

where V_θ is the average open-circuit voltage peak under bending angle θ and V_{90° is the average open-circuit voltage peak when θ is 90°. Because the geometric parameters of the honeycomb piezoelectric network determine the elastic modulus and Poisson's ratio of the structure, the electrical responses as well as η_θ vary for different geometry of piezoelectric network due to direct piezoelectric effect. Through the theoretical investigation of the relations of the equivalent elastic modulus and Poisson's ratio with the parameters *h*, *l*, and α (Fig. 3A), we can observe that the ratio of equivalent elastic modulus E_1 along 0° over E_2 along 90° tends to reach the maximum when α is close to 0° (figs. S7 and S8 and text S3), which represents the highest anisotropy.

To further elucidate the effects of the honeycomb geometry, bending angle, and bending radius on the mechanical and electrical responses, a finite element analysis (FEA) is conducted using COMSOL Multiphysics version 5.5 (detailed information can be found in text S4). Figure 3B shows the strain distributions of the ceramic network under 0° and 90° bending angle for three different geometric parameters, which are in accordance with the mentioned cases of 0, 10, and 20% prestrain. We observe that the strain difference under 0° and 90° bending angle rises substantially with higher prestrain, indicating that the anisotropy is largely enhanced for the 20% prestrain case compared to the other two cases. Besides, the strain in the 0° direction is higher than that in the 90° direction. The variation of the electrical signal shows a similar trend with the strain. From Fig. 3C and fig. S9, it can be concluded that: (i) the high prestrain, which corresponds to the smaller α, leads to the enhancement of the anisotropic piezoelectric responses; (ii) the electrical signal monotonously decreases with a larger bending angle θ and a larger bending radius of curvature *r*; and (iii) η_{0° is more than 10 for the 20% prestrain case, while it is only 1.8 for 0% prestrain case under the bending radius of 20 mm.

Figure 3 (D and E) and fig. S10 show the experimental results of the piezoelectric responses of the S-HAPNC sensor based on the template with the prestrain of 0, 10, and 20% under different bending radii (20, 25, 30, 35, and 40 mm) and different bending angles (0°, 22.5°, 45°, 67.5°, and 90°) (detailed characterization method can be found in text S2). The experimental results show a consistent tendency with the simulation (FEA) results to a certain extent, regardless of the value difference due to the experimental errors and the simplification in simulation (Fig. 3C). The consistency of the piezoelectric responses among different samples is shown in fig. S11. In the experiments, the maximum output voltages are 382, 653, and 945 mV for the case of 0, 10, and 20%, respectively. The improvement of the maximum output voltage results from the increase of effective mass of the PZT ceramic network per unit volume with prestrain rising from 0 to 20%. Furthermore, η_{0° increases from 2 to 17.3 under a 20-mm bending radius when the prestrain increases from 0 to 20% (Fig. 3C), revealing the enhancement of the piezoelectric anisotropy of the S-HAPNC sensor, which is much higher than that of the anisotropic sensors previously reported (detailed comparison has been summarized in Fig. 3F and table S1) (*45*–*50*).

Simultaneous recognition of the bending radius and the bending angle

The piezoelectric anisotropy of the HAPNC sensor helps the simultaneous recognition of bending radius and bending angle. Because the open-circuit voltage signal is determined by both bending radius and bending angle under the same geometric configuration, the double-layer HAPNC with the top and bottom sensors, whose alignments are arranged to be perpendicular, is used to derive bending radius and bending angle.

Figure 4A shows the circuit connection, the polarization direction, the bending angle θ, and the bending radius r. With the consideration of its highly anisotropic piezoelectric responses, we choose the HAPNC sensor based on the template with a 20% prestrain in the following experiments. Figure S12 shows the experimental results of the top and bottom sensors under different bending radii and bending angles. As expected, the piezoelectric responses of the top and bottom sensors show opposite variation tendency with the bending angle θ. The average open-circuit voltage peak of the bottom sensor reaches its maximum at 0°, while it is 90° for the top sensor. Besides, because of the strain difference during the bending process, the top sensor has a relatively larger piezoelectric response along the most effective direction (90°) compared to the piezoelectric response of the bottom sensor at 0°.

To obtain the bending radius and bending angle from the piezoelectric responses of the top and bottom sensors, we define their relation by a function set, i.e.

$$V_{\text{bottom}} = a_1(\cos\theta + b_1)(r + c_1) \quad (2)$$

$$V_{\text{top}} = a_2(\cos\theta + b_2)(r + c_2) \quad (3)$$

where V_{bottom} and V_{top} are the open-circuit voltage peak of the top and bottom sensors, respectively, and a_1, b_1, c_1, a_2, b_2, and c_2 are the coefficients. Figure 4 (B and C) shows the fitting results of the top and bottom sensors based on the experimental results (detailed fitting equations can be found in text S5). In the fitting model, R^2 values are 0.971 for the top sensor and 0.938 for the bottom sensor, which indicates the strong correlation between the fitting results and experimental results. Thus, once the piezoelectric responses (i.e., V_{bottom} and V_{top}) from the top and bottom sensors are obtained, we can accordingly obtain the bending angle θ and the bending radius r.

To monitor the finger movements and joint motions of hand, the HAPNC sensor is attached to the skin surface of palm. With five fingers moving, the HAPNC sensor is bent at a specific direction and corresponding piezoelectric responses are produced from the top and bottom sensors (Fig. 4, D to F). By solving the equations (Eqs. 2 and 3), the bending angle θ and the bending radius r from joint motion of palm can be obtained, fitting well with the experiments. During the durability test, the piezoelectric responses of the top and bottom sensors keep an excellent stability under 10,000 bending cycles while demonstrating a decline after 20,000 bending cycles (fig. S13, A and B). As a result, the calculated result shows a difference from the experimental data after the 20,000 bending cycles (fig. S13, C and D), and a further calibration needs to be conducted (detailed information can be found in table S2 and text S5).

Joint motion monitoring and alarm system

With the aid of the piezoelectric anisotropy, we use the HAPNC sensor to monitor the joint motions deriving from neck or limb movements with multiple degrees of freedom. As illustrated in Fig. 5A, four typical movements for the human neck include twisting to right, twisting to left, stretching to back, and stretching to front. For the human shoulder shown in Fig. 5B, the moving forward, backward, and outward of upper arm occur. To identify different motion modes, the double-layer HAPNC sensors are attached to the skin surface of joints in the arrangement of "X." When the

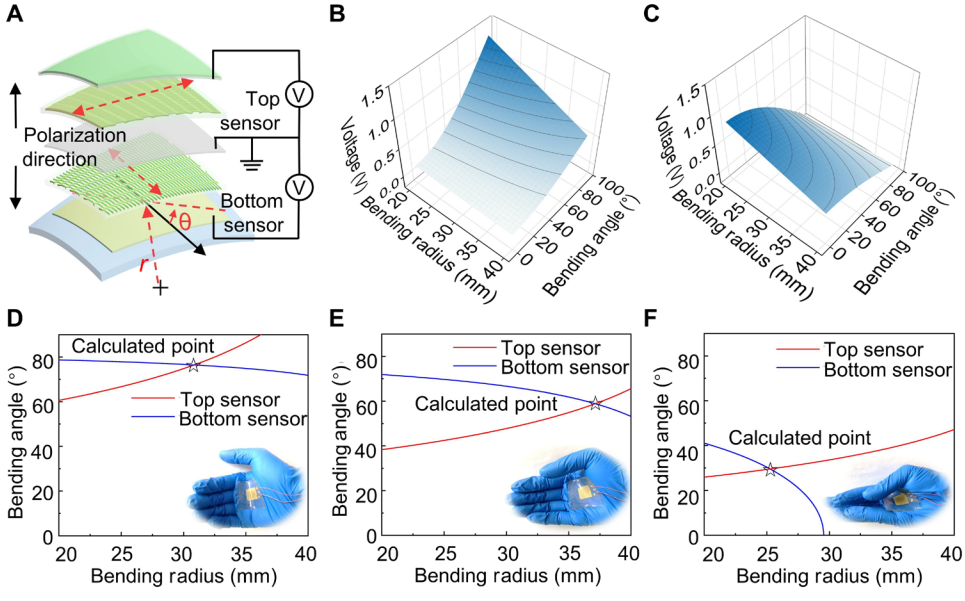

Fig. 4. Simultaneous recognition of the bending radius and the bending angle. (**A**) Illustration showing the bending angle and the bending radius of the double-layer HAPNC sensor with the top and bottom sensors. (**B**) 3D fitting result of the piezoelectric responses from the top sensor based on the experimental data. (**C**) 3D fitting result of the piezoelectric responses from the bottom sensor based on the experimental data. (**D** to **F**) Demonstration of the hand movement detection using the HAPNC sensor. The coordinates of the intersection point of two contour curves reveal the bending angle and the bending radius, consistent with the experiments in the insets.

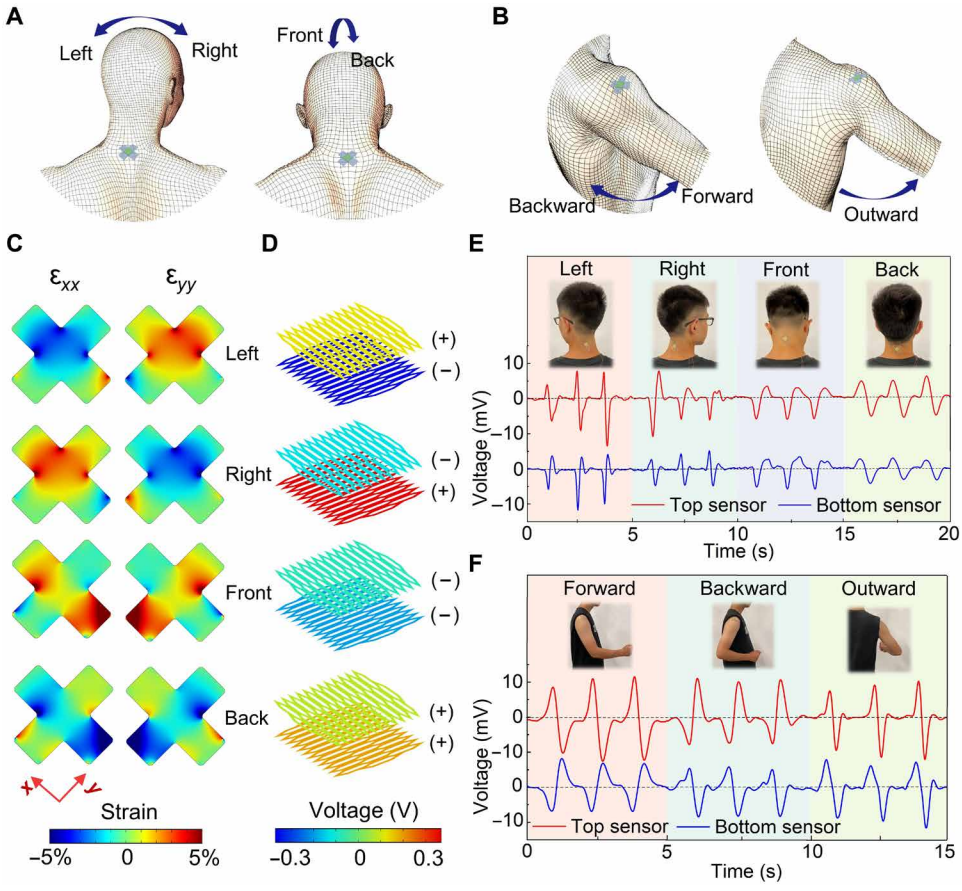

Fig. 5. Working mechanism of HAPNC sensor for joint motion monitoring. (**A**) Schematic diagram of four typical movements of human neck, including twisting to left, twisting to right, stretching to front, and stretching to back. (**B**) Illustration of shoulder motions from upper arm elevation, including moving forward, backward, and outward. (**C**) Simulation results showing the strain fields of PET substrate under four basic deformations. (**D**) Corresponding calculated voltages of the top and bottom sensors. (**E** and **F**) Experimental results of the piezoelectric signals produced from (E) neck motions and (F) shoulder motions. Photo credit: Ying Hong, City University of Hong Kong.

joints move, the substrate of the HAPNC sensor deforms in four basic modes, as shown in fig. S14.

On the basis of the FEA illustrated in Fig. 5 (C and D), we find that each deformation mode corresponds to different strain state and specific electrical signals, which allows us to identify different deformation modes from the output voltages of the HAPNC sensor. For example, when neck twists to left or shoulder moves forward, the strain in the *x* direction is compressive and that in the *y* direction is tensile. This type of strain state further leads to the positive electrical signal from the top sensor and the negative electrical signal from the bottom sensor. The relations between different joint motions and the electrical signals from the top and bottom sensors are summarized in table S3, which is further validated by the experiments of the joint motions from human neck and shoulder.

Figure 5E and movie S1 show the experimental results from different joint motions of human neck. With neck moving to different directions, the top and bottom sensors produce different electrical signals, showing the same tendency with the simulation results. When neck twists to left, the piezoelectric signal is positive (bending process) and then negative (releasing process) for the top sensor, while it is negative and then positive for the bottom sensor. When neck twists to right, the piezoelectric signal is negative and then positive for the top sensor, while it is positive and then negative for the bottom sensor. Besides, the piezoelectric signals are negative and then positive for both the top and bottom sensors when neck stretches to front, while the piezoelectric signals are negative and then positive for both the top and bottom sensors when neck stretches to back. The experimental results from different joint motions of human shoulder are shown in Fig. 5F and movie S2, which also agree with the simulation results.

To further verify the viability of joint motion monitoring of the HAPNC sensors, the piezoelectric signals from the top and bottom sensors are collected and analyzed through LabVIEW 2019 (detailed analysis process can be found in figs. S15 and S16). Figure 6A and movies S3 show the electrical signals of the HAPNC sensor attached on the neck during 100-s neck moving, and the recognition accuracy is more than 95%. The two missing captures are ascribed to the inadequate motion amplitudes, which leads the electrical signal under the threshold of judgment. Figure 6B and movie S4 show the piezoelectric signals of the HAPNC sensor attached on the shoulder during 100-s arm moving, and the recognition accuracy is also more than 95%.

On the basis of the high capture accuracies of the joint motion from the HAPNC sensors, a monitoring and alarm system is

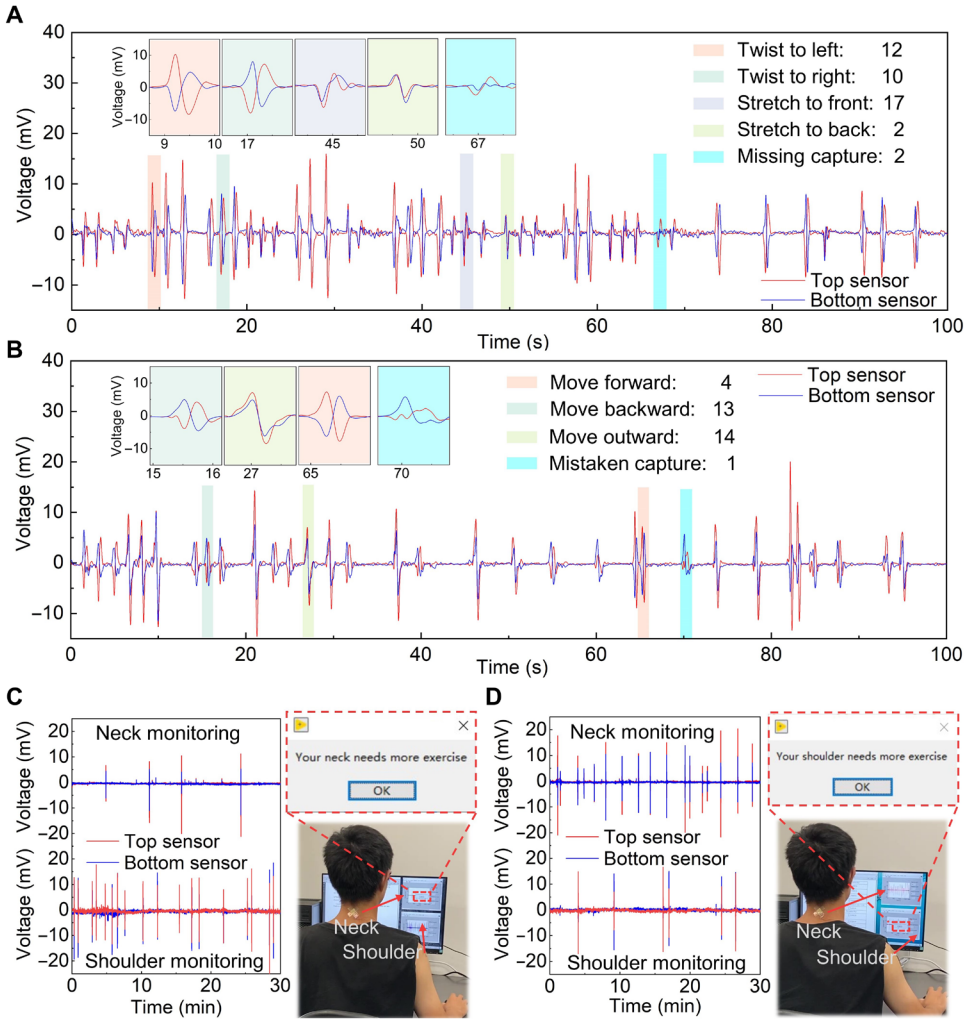

Fig. 6. Joint motion monitoring and alarm system. (**A** and **B**) Piezoelectric signals of the HAPNC sensor attached on (A) neck during 100-s neck moving, and (B) shoulder during 100-s arm moving. Insets show the magnified signals from different motions, as well as the motion capture and recognition. (**C** and **D**) Piezoelectric signals from neck and shoulder motions in 30 min and the pop-up reminder when neck and shoulder need more stimulation, respectively. Photo credit: Ying Hong, City University of Hong Kong.

developed to remind the user to relax after prolonged sedentary work. The piezoelectric signals in 30 min are collected and then judged by the monitoring and alarm system. If the captured movements are less than a certain times in one testing period, a window displaying "your neck needs more exercise" or "your shoulder needs more exercise" will pop up on the computer screen.

In the experiments, a tester sits in front of a computer with the HAPNC sensors attached on the neck and shoulder, and the produced electrical signals are simultaneously transmitted to the computer through a microcontroller. The threshold is set to 10 times in 30 min. Figure 6 (C and D) shows the two types of experimental results of the alarm system. In the first case, the captured movements of neck are more than 10 times, while the captured movements of shoulder are less than 10 times in 30 min. Thus, a window displaying "your shoulder needs more exercise" pops up on the computer screen (Fig. 6C and movie S5). In the second case, the captured movements of neck are less than 10 times, while the captured movements of shoulder are more than 10 times. Thus, a window displaying "your neck needs more exercise" subsequently pops up on the computer screen (Fig. 6D and movie S6). These experiments reveal that the monitoring and alarm system based on the HAPNC sensor is capable of monitoring the joint motions of neck and shoulder and alarming the prolonged sedentary behavior.

DISCUSSION

In this study, we demonstrate a functional piezoelectric kirigami with a large measurement range and highly anisotropic piezoelectric responses, which is further used to monitor the motions from human joints. A modified template-assisted sol-gel material fabrication method is developed, which is simple, controllable, and effective in manufacturing high-quality stretchable piezoelectric composite with increased connectivity of the piezoceramic phase. Compared to the anisotropic bending sensors previously reported, the developed HAPNC sensor has a high sensitivity and excellent anisotropic piezoelectric response attributed to the well-aligned kirigami-structured piezoceramic network. During the manufacturing of the piezoelectric kirigami composite, prestretching the

honeycomb textile template yields a high-level alignment of the piezoceramic network and correspondingly an enhanced piezoelectric anisotropy, which has been verified by theoretical and experimental studies. Using this piezoelectric anisotropy, we establish the relation of the bending direction and the bending radius to the electrical signals of the HAPNC sensor, facilitating the analysis of human hand motion. Once the HAPNC sensor is attached to human neck and shoulder, it has the ability to identify four types of deformation modes from joint motions with the 95% recognition accuracy. On the basis of this property, a monitoring and alarm system is developed to monitor the joint motions of neck and shoulder in a long time, helping to ameliorate the prolonged sedentary behavior.

As demonstrated above, the developed HAPNC sensor offers a number of advantages, including large measurement range, high piezoelectric anisotropy, multifunctional measurement abilities, and long-term monitoring capability. The concept of designing anisotropic kirigami and manufacturing functional piezoceramic network provides a new solution for the emerging stretchable multifunctional piezoelectric devices. The strategy of fabricating highly anisotropic bending sensors and monitoring joint motions with such sensor will also promote the development of flexible electronics in health monitoring devices and the prevention and rehabilitation of upper extremity MSDs.

MATERIALS AND METHODS

Preparation of the aligned PZT ceramic network

The nylon textile with honeycomb grids (15 mm length, 7.5 mm width) is purchased from market and tailored to specific shape (9 cm × 3 cm). The as-prepared mixed PZT suspensions are then dropped onto the stretched organic textile until the whole organic textile template is immersed by the mixed suspensions. After hot air drying, the sol immersed in textile converts to gel. The precursor is then sintered to remove the organic templates and the aligned PZT ceramic network is thus obtained (details of the fabrication appear in text S1 and fig. S1).

Preparation of the kirigami-structured HAPNC sensor

The prepared uncured PDMS is spin-coated onto the surface of a PET film with an ITO film. With the PZT ceramic network fully infiltrated by the uncured PDMS film, the obtained PZT network composite is then cured. Followed by spraying the bottom Ag NW electrode, the composite is spin-coated with another uncured PDMS layer. Then, a PZT ceramic network with perpendicular alignment is attached to the surface of uncured PDMS. Fully infiltrated and cured, the obtained composite is sprayed with Ag NWs to form the top electrode, with PDMS spin-coated onto the surface as the protective layer (details of the fabrication appear in text S1 and fig. S1).

Piezoelectric characterization of the HAPNC sensor

The tapping test is conducted by a vibration generator, with a controllable oscillation frequency and tapping force. The tapping force, which is detected and quantified by mechanical force sensors, is adjusted by the distance between the tapping pillar and sample surface. The bending test is conducted by a motor and linear guideway. Two ends of the sample are fixed to the built-in end and mobile end of the liner guideway, respectively. Once actuated by the motor, the sample is continuously bended and released, producing an electrical response. The bending radius is controlled by the displacement of the mobile end of the liner guideway.

Theoretical analysis of the anisotropic honeycombs

The anisotropy of the honeycomb structures is described by an analytical theory. The equivalent elastic modulus of the honeycombs is directly derived using the basic definition. Because piezoelectric materials are transversely isotropic, here, we focus on the stiffness and Poisson's ratio in the plane perpendicular to the polarization direction. Considering the honeycomb composed of periodically arrayed hexagons as shown in fig. S7A, each hexagon contains two kinds of cell walls, with the length l and h, the angle α, the thickness t_0 and t_1, the depth b, and the Young's modulus E_p. The walls are modeled as a beam without the consideration of shear deformation (details of the analysis appear in text S3).

FEA of the HAPNC sensor

The FEA is conducted to obtain the mechanical and electrical responses of HAPNC sensor. In the framework of stationary theory, we only take the linear elastics and piezoelectric effects into account. In the finite element modeling, the PET substrate and PDMS matrix are modeled as isotropic elastic materials without piezoelectric effect, while anisotropy and piezoelectricity are considered in the PZT material. Thus, the continuous conditions between all interfaces are used. Finite element model is then solved with the consideration of equilibrium equations and boundary conditions (details of the analysis appear in text S4).

Fitting results of the piezoelectric signals

According to the data from the experiments (fig. S12), the fitting results for the top and bottom sensors are shown as

$$V_{top} = 2.0375 - 1.8572\cos\theta - 0.0359r + 0.0336r \cdot \cos\theta \quad (4)$$

$$V_{bottom} = -0.1016 + 1.411\cos\theta + 0.0029r - 0.0259r \cdot \cos\theta \quad (5)$$

Once the piezoelectric responses (i.e., V_{bottom} and V_{top}) are obtained, we can get the corresponding bending angle θ and bending radius r from joint strain of palm by solving the equations (Eqs. 4 and 5). Two contours are drawn in the plane according to the equation set, as shown in Fig. 4 (D to F). From the coordinates of the intersection point of these two curves, bending angle θ and bending radius r are calculated as listed in table S3 (details of the fitting results appear in text S5).

SUPPLEMENTARY MATERIALS

Supplementary material for this article is available at http://advances.sciencemag.org/cgi/content/full/7/11/eabf0795/DC1

REFERENCES AND NOTES

1. C. A. Kennedy, B. C. Amick III, J. T. Dennerlein, S. Brewer, S. Catli, R. Williams, C. Serra, F. Gerr, E. Irvin, Q. Mahood, A. Franzblau, D. Van Eerd, B. Evanoff, D. Rempel, Systematic review of the role of occupational health and safety interventions in the prevention of upper extremity musculoskeletal symptoms, signs, disorders, injuries, claims and lost time. *J. Occup. Rehabil.* **20**, 127–162 (2010).
2. D. A. J. Salvagioni, F. N. Melanda, A. E. Mesas, A. D. Gonzalez, F. L. Gabani, S. M. de Andrade, Physical, psychological and occupational consequences of job burnout: A systematic review of prospective studies. *PLOS ONE* **12**, e0185781 (2017).
3. S. Bevan, Economic impact of musculoskeletal disorders (MSDs) on work in Europe. *Best Pract. Res. Clin. Rheumatol.* **29**, 356–373 (2015).

4. D. Jun, M. Zoe, V. Johnston, S. O'Leary, Physical risk factors for developing non-specific neck pain in office workers: A systematic review and meta-analysis. *Int. Arch. Occup. Environ. Health* **90**, 373–410 (2017).
5. H. F. van der Molen, C. Foresti, J. G. Daams, M. H. W. Frings-Dresen, P. P. F. M. Kuijer, Work-related risk factors for specific shoulder disorders: A systematic review and meta-analysis. *Occup. Environ. Med.* **74**, 745–755 (2017).
6. D. Van Eerd, C. Munhall, E. Irvin, D. Rempel, S. Brewer, A. J. Van der Beek, J. T. Dennerlein, J. Tullar, K. Skivington, C. Pinion, B. Amick, Effectiveness of workplace interventions in the prevention of upper extremity musculoskeletal disorders and symptoms: An update of the evidence. *Occup. Environ. Med.* **73**, 62–70 (2016).
7. A. Faisal, S. Majumder, T. Mondal, D. Cowan, S. Naseh, M. J. Deen, Monitoring methods of human body joints: State-of-the-art and research challenges. *Sensors* **19**, 2629 (2019).
8. D. Lo Presti, A. Carnevale, J. D'Abbraccio, L. Massari, C. Massaroni, R. Sabbadini, M. Zaltieri, J. Di Tocco, M. Bravi, S. Miccinilli, S. Sterzi, U. G. Longo, V. Denaro, M. A. Caponero, D. Formica, C. M. Oddo, E. Schena, A multi-parametric wearable system to monitor neck movements and respiratory frequency of computer workers. *Sensors* **20**, 536 (2020).
9. B. H. Wang, A. Thukral, Z. Q. Xie, L. M. Liu, X. N. Zhang, W. Huang, X. G. Yu, C. J. Yu, T. J. Marks, A. Facchetti, Flexible and stretchable metal oxide nanofiber networks for multimodal and monolithically integrated wearable electronics. *Nat. Commun.* **11**, 2405 (2020).
10. R. Z. Lin, H.-J. Kim, S. Achavananthadith, S. A. Kurt, S. C. C. Tan, H. Yao, B. C. K. Tee, J. K. W. Lee, J. S. Ho, Wireless battery-free body sensor networks using near-field-enabled clothing. *Nat. Commun.* **11**, 444 (2020).
11. J. Kim, A. S. Campbell, B. E.-F. de Avila, J. Wang, Wearable biosensors for healthcare monitoring. *Nat. Biotechnol.* **37**, 389–406 (2019).
12. X. Tian, P. M. Lee, Y. J. Tan, T. L. Y. Wu, H. C. Yao, M. Y. Zhang, Z. P. Li, K. A. Ng, B. C. K. Tee, J. S. Ho, Wireless body sensor networks based on metamaterial textiles. *Nat. Electron.* **2**, 243–251 (2019).
13. T. He, H. Wang, J. Wang, X. Tian, F. Wen, Q. Shi, J. S. Ho, C. Lee, Self-sustainable wearable textile nano-energy nano-system (NENS) for next-generation healthcare applications. *Adv. Sci.* **6**, 1901437 (2019).
14. Y. Liu, M. Pharr, G. A. Salvatore, Lab-on-skin: A review of flexible and stretchable electronics for wearable health monitoring. *ACS Nano* **11**, 9614–9635 (2017).
15. T. Someya, Z. N. Bao, G. G. Malliaras, The rise of plastic bioelectronics. *Nature* **540**, 379–385 (2016).
16. A. Chortos, J. Liu, Z. A. Bao, Pursuing prosthetic electronic skin. *Nat. Mater.* **15**, 937–950 (2016).
17. Y. Yamamoto, S. Harada, D. Yamamoto, W. Honda, T. Arie, S. Akita, K. Takei, Printed multifunctional flexible device with an integrated motion sensor for health care monitoring. *Sci. Adv.* **2**, e1601473 (2016).
18. S. Xu, Y. Zhang, L. Jia, K. E. Mathewson, K.-I. Jang, J. Kim, H. Fu, X. Huang, P. Chava, R. Wang, S. Bhole, L. Wang, Y. J. Na, Y. Guan, M. Flavin, Z. Han, Y. Huang, J. A. Rogers, Soft microfluidic assemblies of sensors, circuits, and radios for the skin. *Science* **344**, 70–74 (2014).
19. K. K. Kim, I. Ha, M. Kim, J. Choi, P. Won, S. Jo, S. H. Ko, A deep-learned skin sensor decoding the epicentral human motions. *Nat. Commun.* **11**, 2149 (2020).
20. S. Mishra, Y.-S. Kim, J. Intarasirisawat, Y.-T. Kwon, Y. Lee, M. Mahmood, H.-R. Lim, R. Herbert, K. J. Yu, C. S. Ang, W.-H. Yeo, Soft, wireless periocular wearable electronics for real-time detection of eye vergence in a virtual reality toward mobile eye therapies. *Sci. Adv.* **6**, eaay1729 (2020).
21. M. K. Kim, C. Kantarcigil, B. Kim, R. K. Baruah, S. Maity, Y. Park, K. Kim, S. Lee, J. B. Malandraki, S. Avlani, A. Smith, S. Sen, M. A. Alam, G. Malandraki, C. H. Lee, Flexible submental sensor patch with remote monitoring controls for management of oropharyngeal swallowing disorders. *Sci. Adv.* **5**, eaay3210 (2019).
22. K.-I. Jang, K. Li, H. U. Chung, S. Xu, H. N. Jung, Y. Yang, J. W. Kwak, H. H. Jung, J. Song, C. Yang, A. Wang, Z. Liu, J. Y. Lee, B. H. Kim, J.-H. Kim, J. Lee, Y. Yu, B. J. Kim, H. Jang, K. J. Yu, J. Kim, J. W. Lee, J.-W. Jeong, Y. M. Song, Y. Huang, Y. Zhang, J. A. Rogers, Self-assembled three dimensional network designs for soft electronics. *Nat. Commun.* **8**, 15894 (2017).
23. B. W. An, S. Heo, S. Ji, F. Bien, J.-U. Park, Transparent and flexible fingerprint sensor array with multiplexed detection of tactile pressure and skin temperature. *Nat. Commun.* **9**, 2458 (2018).
24. W. Fan, Q. He, K. Meng, X. Tan, Z. Zhou, G. Zhang, J. Yang, Z. L. Wang, Machine-knitted washable sensor array textile for precise epidermal physiological signal monitoring. *Sci. Adv.* **6**, eaay2840 (2020).
25. E. O. Polat, G. Mercier, I. Nikitskiy, E. Puma, T. Galan, S. Gupta, M. Montagut, J. J. Piqueras, M. Bouwens, T. Durduran, G. Konstantatos, S. Goossens, F. Koppens, Flexible graphene photodetectors for wearable fitness monitoring. *Sci. Adv.* **5**, eaaw7846 (2019).
26. C. M. Boutry, L. Beker, Y. Kaizawa, C. Vassos, H. Tran, A. C. Hinckley, R. Pfattner, S. Niu, J. Li, J. Claverie, Z. Wang, J. Chang, P. M. Fox, Z. Bao, Biodegradable and flexible arterial-pulse sensor for the wireless monitoring of blood flow. *Nat. Biomed. Eng.* **3**, 47–57 (2019).
27. H. Lee, E. Kim, Y. Lee, H. Kim, J. Lee, M. Kim, H.-J. Yoo, S. Yoo, Toward all-day wearable health monitoring: An ultralow-power, reflective organic pulse oximetry sensing patch. *Sci. Adv.* **4**, eaas9530 (2018).
28. M. Bariya, H. Y. Y. Nyein, A. Javey, Wearable sweat sensors. *Nat. Electron.* **1**, 160–171 (2018).
29. S. Emaminejad, W. Gao, E. Wu, Z. A. Davies, H. Y. Y. Nyein, S. Challa, S. P. Ryan, H. M. Fahad, K. Chen, Z. Shahpar, S. Talebi, C. Milla, A. Javey, R. W. Davis, Autonomous sweat extraction and analysis applied to cystic fibrosis and glucose monitoring using a fully integrated wearable platform. *Proc. Natl. Acad. Sci. U.S.A.* **114**, 4625–4630 (2017).
30. W. Gao, S. Emaminejad, H. Y. Y. Nyein, S. Challa, K. Chen, A. Peck, H. M. Fahad, H. Ota, H. Shiraki, D. Kiriya, D.-H. Lien, G. A. Brooks, R. W. Davis, A. Javey, Fully integrated wearable sensor arrays for multiplexed in situ perspiration analysis. *Nature* **529**, 509–514 (2016).
31. D. B. Kim, K. H. Park, Y. S. Cho, Origin of high piezoelectricity of inorganic halide perovskite thin films and their electromechanical energy-harvesting and physiological currentsensing characteristics. *Energ. Environ. Sci.* **13**, 2077–2086 (2020).
32. H. Cui, R. Hensleigh, D. Yao, D. Maurya, P. Kumar, M. G. Kang, S. Priya, X. Zheng, Three-dimensional printing of piezoelectric materials with designed anisotropy and directional response. *Nat. Mater.* **18**, 234–241 (2019).
33. M. D. Han, H. Wang, Y. Yang, C. Liang, W. Bai, Z. Yan, H. Li, Y. Xue, X. Wang, B. Akar, H. Zhao, H. Luan, J. Lim, I. Kandela, G. A. Ameer, Y. Zhang, Y. Huang, J. A. Rogers, Three-dimensional piezoelectric polymer microsystems for vibrational energy harvesting, robotic interfaces and biomedical implants. *Nat. Electron.* **2**, 26–35 (2019).
34. S. Park, S. W. Heo, W. Lee, D. Inoue, Z. Jiang, K. Yu, H. Jinno, D. Hashizume, M. Sekino, T. Yokota, K. Fukuda, K. Tajima, T. Someya, Self-powered ultra-flexible electronics via nano-grating-patterned organic photovoltaics. *Nature* **561**, 516–521 (2018).
35. Z. Yang, S. Zhou, J. Zu, D. Inman, High-performance piezoelectric energy harvesters and their applications. *Joule* **2**, 642–697 (2018).
36. Q. Zheng, B. J. Shi, Z. Li, Z. L. Wang, Recent progress on piezoelectric and triboelectric energy harvesters in biomedical systems. *Adv. Sci.* **4**, 1700029 (2017).
37. C. Dagdeviren, F. Javid, P. Joe, T. von Erlach, T. Bensel, Z. Wei, S. Saxton, C. Cleveland, L. Booth, S. M. Donnell, J. Collins, A. Hayward, R. Langer, G. Traverso, Flexible piezoelectric devices for gastrointestinal motility sensing. *Nat. Biomed. Eng.* **1**, 807–817 (2017).
38. Y. Tang, G. Lin, S. Yang, Y. K. Yi, R. D. Kamien, J. Yin, Programmable kiri-kirigami metamaterials. *Adv. Mater.* **29**, 1604262 (2017).
39. P.-Y. Chen, M. Liu, Z. Wang, R. H. Hurt, I. Y. Wong, From flatland to spaceland: Higher dimensional patterning with two-dimensional materials. *Adv. Mater.* **29**, 1605096 (2017).
40. M. K. Blees, A. W. Barnard, P. A. Rose, S. P. Roberts, K. L. McGill, P. Y. Huang, A. R. Ruyack, J. W. Kevek, B. Kobrin, D. A. Muller, P. L. McEuen, Graphene kirigami. *Nature* **524**, 204–207 (2015).
41. Y. Zhang, F. Zhang, Z. Yan, Q. Ma, X. Li, Y. Huang, J. A. Rogers, Printing, folding and assembly methods for forming 3D mesostructures in advanced materials. *Nat. Rev. Mater.* **2**, 17019 (2017).
42. G. Zhang, P. Zhao, X. Zhang, K. Han, T. Zhao, Y. Zhang, C. K. Jeong, S. Jiang, S. Zhang, Q. Wang, Flexible three-dimensional interconnected piezoelectric ceramic foam based composites for highly efficient concurrent mechanical and thermal energy harvesting. *Energ. Environ. Sci.* **11**, 2046–2056 (2018).
43. H. Lu, Y. Hong, Y. Yang, Z. Yang, Y. Shen, Battery-less soft millirobot that can move, sense, and communicate remotely by coupling the magnetic and piezoelectric effects. *Adv. Sci.* **7**, 2000069 (2020).
44. M. Xie, Y. Zhang, M. J. Kraśny, C. Bowen, H. Khanbareh, N. Gathercole, Flexible and active self-powered pressure, shear sensors based on freeze casting ceramic-polymer composites. *Energ. Environ. Sci.* **11**, 2919–2927 (2018).
45. H. Chen, Z. Su, Y. Song, X. Cheng, X. Chen, B. Meng, Z. Song, D. Chen, H. Zhang, Omnidirectional bending and pressure sensor based on stretchable CNT-PU sponge. *Adv. Funct. Mater.* **27**, 1604434 (2017).
46. S. Huang, G. He, C. Yang, J. Wu, C. Guo, T. Hang, B. Li, C. Yang, D. Liu, H.-J. Chen, Q. Wu, X. Gui, S. Deng, Y. Zhang, F. Liu, X. Xie, Stretchable strain vector sensor based on parallelly aligned vertical graphene. *ACS Appl. Mater. Interfaces* **11**, 1294–1302 (2019).
47. S. Chen, Y. Song, D. Ding, Z. Ling, F. Xu, Flexible and anisotropic strain sensor based on carbonized crepe paper with aligned cellulose fibers. *Adv. Funct. Mater.* **28**, 1802547 (2018).
48. S. R. Kim, J. H. Yoo, Y. S. Cho, J. W. Park, Flexible piezoelectric energy generators based on P(VDF-TrFE) nanofibers. *Mater. Res. Express* **6**, 086311 (2019).
49. H.-J. Lee, S. Y. Chung, Y. S. Kim, T. I. Lee, Nonlinear piezoelectric dual sensor for the detection of angle and radius of a bending deformation. *Nano Energy* **38**, 232–238 (2017).
50. H. Lee, H. Kim, D. Y. Kim, Y. Seo, Pure piezoelectricity generation by a flexible nanogenerator based on lead zirconate titanate nanofibers. *ACS Omega* **4**, 2610–2617 (2019).

51. E. J. Lee, T. Y. Kim, S.-W. Kim, S. Jeong, Y. Choi, S. Y. Lee, High-performance piezoelectric nanogenerators based on chemically-reinforced composites. *Energ. Environ. Sci.* **11**, 1425–1430 (2018).
52. L. J. Gibson, M. F. Ashby, G. S. Schajer, C. I. Robertson, The mechanics of two-dimensional cellular materials. *Proc. R. Soc. Lond. A* **382**, 25–42 (1982).
53. A. Erturk, D. J. Inman, *Piezoelectric Energy Harvesting* (John Wiley & Sons, 2011).

Acknowledgments
Funding: We acknowledge the financial support from the Early Career Scheme from the Research Grants Council of Hong Kong (project no. 21210619), the National Natural Science Foundation of China (no. 11902282), and the City University of Hong Kong (no. 9610390).
Ethics statement: All procedures performed in the study involving human participants were approved by the Human Subjects Ethics Committee of the City University of Hong Kong (reference no. 1-2021-26-E). All subjects were informed of the risks and benefits and provided informed consent. **Author contributions:** Z.Y. and Y.H. conceived the project and designed the studies. Y.H., B.W., L.J., and S.L. performed experiments and analyzed the experimental data. B.W. worked on structure design and mechanics modeling, with assistance from W.L. in circuit design. Y.H., B.W., X.L., J.P., W.W., and Z.Y. composed the manuscript. **Competing interests:** The authors declare that they have no competing interests. **Data and materials availability:** All data needed to evaluate the conclusions in the paper are present in the paper and/or the Supplementary Materials. Additional data related to this paper may be requested from the authors.

Submitted 3 October 2020
Accepted 27 January 2021
Published 12 March 2021
10.1126/sciadv.abf0795

Citation: Y. Hong, B. Wang, W. Lin, L. Jin, S. Liu, X. Luo, J. Pan, W. Wang, Z. Yang, Highly anisotropic and flexible piezoceramic kirigami for preventing joint disorders. *Sci. Adv.* **7**, eabf0795 (2021).

Highly anisotropic and flexible piezoceramic kirigami for preventing joint disorders

Ying Hong, Biao Wang, Weikang Lin, Lihan Jin, Shiyuan Liu, Xiaowei Luo, Jia Pan, Wenping Wang and Zhengbao Yang

Sci Adv **7** (11), eabf0795.
DOI: 10.1126/sciadv.abf0795